

## Effects of shock parameters on upstream energetic electron burst events

Xingqiu Yuan,<sup>1,2</sup> Iver H. Cairns,<sup>1</sup> Larisa Trichtchenko,<sup>2</sup> and Robert Rankin<sup>3</sup>

Received 11 April 2008; revised 5 June 2008; accepted 20 June 2008; published 9 September 2008.

[1] Recent simulation results have revealed that energetic electron bursts are produced cyclically at the shock reformation period upstream of reforming shocks and are qualitatively very different from the continuous beam expected from time-stationary shocks (Yuan et al., 2007a). This paper extends our previous studies by numerically investigating the dependence of electron burst events on shock parameters (the upstream plasma  $\beta$  and Mach number  $M_A$ ). The test particle approximation is made for electrons, and the electron trajectories are traced exactly in the time-dependent electromagnetic field profiles, generated by one-dimensional hybrid simulation code. Simulation results indicate that the upstream incoming electrons can be reflected nonuniformly or continuously depending on the shock parameters. Bursty energetic electron events take place when the plasma beta is low ( $\beta \leq 0.4$ ) and the shock Mach number is high ( $M_A \geq 6$ ). Time-varying loss cone, beam, and ring beam features are observed in the upstream electron distribution functions. The beam density, speed, average kinetic energy, and speed spread cyclically change with time by factor of  $\sim 2-4$ . In contrast, continuously reflected electrons are observed for low beta ( $\beta \leq 0.4$ ), low Mach number ( $M_A \leq 4$ ) shocks, even when the shock is reforming because the changes in shock fields are relative small. The electron burst events disappear and the observed upstream electron distribution function contours are steady state. A continuous electron beam is formed, which is qualitative the same as the beam from steady-state shocks. Increasing the plasma beta (providing the shock is still reforming) has minor effects on the upstream electron beam features.

**Citation:** Yuan, X., I. H. Cairns, L. Trichtchenko, and R. Rankin (2008), Effects of shock parameters on upstream energetic electron burst events, *J. Geophys. Res.*, 113, A09106, doi:10.1029/2008JA013309.

### 1. Introduction

[2] Spacecraft observations have shown that a small fraction of solar wind electrons can be accelerated to energies ranging from several to 100 keV at planetary bow shocks, interplanetary shocks, and coronal mass ejection-driven shocks [Fan et al., 1964; Anderson, 1969, 1981; Anderson et al., 1979; Parks et al., 1981; Johns and Lin, 1992]. These electrons are responsible for various plasma waves and emissions [Filbert and Kellogg, 1979; Cairns and Fung, 1988; Knock et al., 2001, 2003; Kuncic et al., 2004]. The electron acceleration mechanism in shocks has been a popular topic during the last 20 years [Leroy and Mangeney, 1984; Wu, 1984; Krauss-Varban et al., 1989; Vandas, 1989a, 1989b; Veltri et al., 1990; Krauss-Varban and Burgess, 1991; Krauss-Varban, 1994; Lowe and Burgess, 2000; Shimada and Hoshino, 2000; Hoshino and Shimada, 2002; Lembége and Savoini, 2002; Burgess, 2006; Yuan et al., 2007a, 2007b, 2007c]. Theoretical analysis [Leroy and

Mangeney, 1984; Wu, 1984] and numerical simulations [Krauss-Varban et al., 1989; Vandas, 1989a, 1989b; Veltri et al., 1990; Krauss-Varban and Burgess, 1991; Krauss-Varban, 1994; Lowe and Burgess, 2000; Shimada and Hoshino, 2000; Hoshino and Shimada, 2002; Lembége and Savoini, 2002; Burgess, 2006; Yuan et al., 2007a, 2007b, 2007c] can explain many features of observed upstream electron distribution functions, including their characteristic loss cone, beam, and ring beam structures and the enhanced high-energy power law tail in the upstream region.

[3] One of the most widely applied shock acceleration models for electrons is shock drift acceleration (SDA) in which the conservation of magnetic moment for reflected electrons is assumed [Leroy and Mangeney, 1984; Wu, 1984]. According to SDA model, the energy of electrons reflected by the shock is conserved in the de Hoffmann–Teller frame (HTF), but the parallel component of velocity is reversed. This change of velocity, as seen in the normal incident frame (NIF) in which the shock is at rest and upstream flow is directed along shock normal into the shock, leads to acceleration of reflected electrons. Physically, this energization process is due to the electrons undergoing a magnetic gradient drift motion antiparallel to the solar wind's motional electric field. This model was tested and confirmed by Krauss-Varban et al. [1989] and Veltri et al. [1990] using numerical simulations. It was also extended to curved shocks

<sup>1</sup>School of Physics, University of Sydney, Sydney, New South Wales, Australia.

<sup>2</sup>Geomagnetic Laboratory, Natural Resource Canada, Ottawa, Ontario, Canada.

<sup>3</sup>Department of Physics, University of Alberta, Edmonton, Alberta, Canada.

by *Vandas* [1989a, 1989b] and *Krauss-Varban and Burgess* [1991]. *Knock et al.* [2001, 2003] introduced a physical model using SDA to explain interplanetary type II radio bursts, while *Kuncic et al.* [2004] produced a similar model for radiation from the Earth's foreshock. However SDA predicts that the highest energies are produced over a very small range of  $\theta_{bn}$  between the shock normal and the upstream magnetic field direction, close to perpendicular angles where the reflected flux is small.

[4] Shock reformation involves large spatial–temporal scale variations of the shock in which the front periodically collapses and develops on a timescale close to the ion cyclotron period. This phenomenon is often observed in one- and two-dimensional computer simulations of high Mach number ( $M_A$ ), low plasma beta ( $\beta \leq 0.4$ ) collisionless shocks [Lembége and Savoini, 1992; Shimada and Hoshino, 2000; Hellinger et al., 2002; Krasnoselskikh et al., 2002; Hada et al., 2003; Scholer et al., 2003; Yuan et al., 2007c]. Strong support for the shock reformation seen in the computer simulations is provided by space observations [Lobzin et al., 2007].

[5] Recent test particle calculations in the self-consistent generated reforming shock fields [Yuan et al., 2007a], and self-consistent full particle simulations [Lembége and Savoini, 2002], have shown that electrons are reflected nonuniformly in time and space by the reforming shock. The energetic electron bursts are produced cyclically at the shock reformation period and nonuniformly trapped in space along the shock front. However, in these previous studies, only one set of typical plasma parameters were used, and the dependence of electron burst events on shock parameters was not studied.

[6] This paper extends the previous simulation results [Yuan et al., 2007a] to investigate the dependence of the upstream electron burst events on shock parameters. The test particle electron trajectories are exactly traced in time-dependent shock profiles self-consistently generated by one-dimensional hybrid code. The simulation results indicate that the reflection of upstream incoming electrons depends strongly on the shock parameters, and electrons can be reflected nonuniformly or continuously. Bursts of energetic electrons occur when the plasma beta is low ( $\beta \leq 0.4$ ), and shock Mach number is high ( $M_A \geq 6$ ). In contrast, continuously reflected electrons are observed for low beta ( $\beta \leq 0.4$ ), low Mach number ( $M_A \leq 4$ ) shocks and the electron burst events disappear, even when the shock is reforming. These differences lead to different features of the electron beam characteristics observed in the upstream region, which will in turn generate different plasma waves. Increasing plasma beta (providing the shock is still reforming) has minor effects on the upstream electron beam features. This paper is organized as follows: section 2 describes the numerical methods used, the main results are given in section 3. A summary and discussion are contained in section 4.

## 2. Numerical Methods

[7] In this paper we use the same code as *Yuan et al.* [2007a]. The piston method is used [Scholer et al., 2003; Burgess, 2006] to produce the time-dependent shock profiles: a high-speed plasma is injected from the left hand boundary and specularly reflected at the right hand bound-

ary. Simulations are performed in the normal incident frame and the upstream magnetic field lies in the  $x$ – $z$  plane at an angle  $\theta_{bn}$  with respect to the  $x$ -axis. This method generates a shock wave propagating to the left of simulation box. The upstream incoming solar wind electrons are described as a Maxwellian core population with a thermal speed ( $v_{the}$ ) determined by the electron plasma beta ( $\beta_e = v_{the}^2/v_A^2$ , where  $v_A$  is upstream Alfvén speed), plus a superthermal halo population. The thermal core electrons are treated as a massless fluid in the hybrid code, while the superthermal halo electrons are treated as test particles [Krauss-Varban et al., 1989; Krauss-Varban and Burgess, 1991; Krauss-Varban, 1994; Burgess, 2006].

[8] The computational domain is  $120c/\omega_{pi}$  long (where  $\omega_{pi}$  is the ion plasma frequency) with 3000 grid points, initially with 200 ions per cell. In order to make the hybrid code run stably, an artificial resistivity  $\eta = 1.0 \times 10^{-2} \mu_0 v_A^2 \Omega_{ci}^{-1}$  is used to damp out some high-frequency waves. This is standard practice for hybrid simulations. However high-frequency electron scale waves are generated in extended hybrid simulations, which include the effects of the electron pressure tensor and finite electron mass [Yuan et al., 2007c], and in PIC simulations [Shimada and Hoshino, 2000; Hoshino and Shimada, 2002; Scholer et al., 2003]. The use of one-dimensional code ignores the high-dimensional effects which may lead to different shock reformation processes [Hellinger et al., 2007]. The effects of these high-frequency waves and higher dimensionality should be considered in the future work.

[9] The test particle simulations are carried out as follows: After the shock is fully developed, electrons are continuously injected into the computational domain at the left boundary. In this paper, we release the test particle electrons from time  $5\Omega_{ci}^{-1}$  ( $\Omega_{ci}$  is the ion gyrofrequency). The random parallel and perpendicular speeds for electrons are drawn from a  $\kappa$  distribution with  $\kappa = 6$  and halo thermal speed  $5v_{the}$  [Krauss-Varban and Burgess, 1991]. No downstream electrons are injected, and electrons cease to be followed when swept out of the computational boundaries. The electron trajectories are computed by numerically integrating the full equations of motion (including gyromotion) using a seventh-order Runge–Kutta method [Evans et al., 2006]. Up to  $5.0 \times 10^7$  electrons are followed in our calculation. We use the time step  $dt = 1.0 \times 10^{-4} \Omega_{ci}^{-1}$  for the ion trajectory calculations, while the time step for integration of the electron equations of motion is  $dt_e = dt/100$ . In order to avoid the unphysical fluctuations caused by spatial and temporal interpolation of electromagnetic fields, we use a second-order spatial interpolation with careful choice of interpolation points, based on the high-resolution essentially nonoscillatory (ENO) scheme widely used in computational gasdynamics [Shu, 1997] and linear interpolation in time between the two adjacent hybrid simulation time steps [Burgess, 2006]. A moving window with width  $3v_A \Omega_{ci}^{-1}$  at a fixed distance of  $v_A \Omega_{ci}^{-1}$  upstream of the shock is set up to observe the upstream electron distribution function.

## 3. Simulation Results

### 3.1. Shock Profiles

[10] Table 1 shows the shock parameters used in this paper, where  $\beta_e$  and  $\beta_i$  are electron and ion plasma beta,

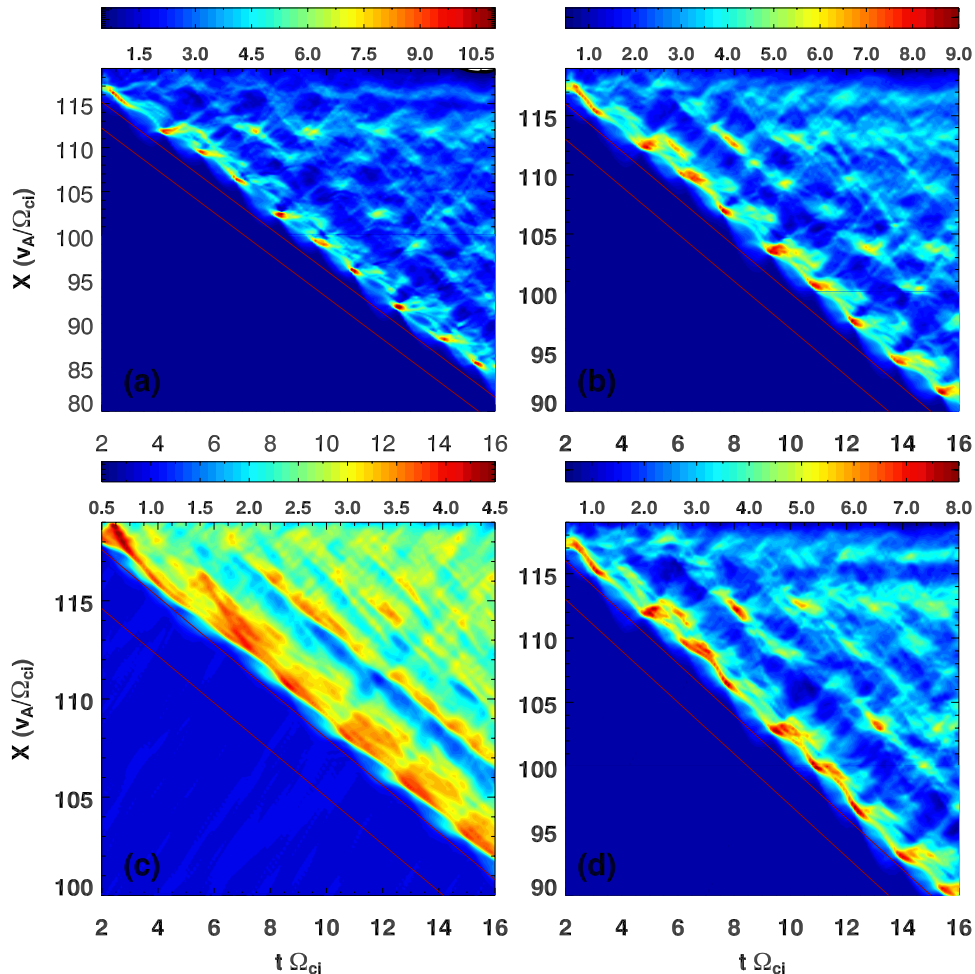
**Table 1.** Shock Parameters of the Cases

Case	$M_A$	$\theta_{bn}$	$\beta_e$	$\beta_i$
a	7.4	$85^\circ$	0.2	0.15
b	6.0	$85^\circ$	0.2	0.15
c	3.2	$85^\circ$	0.2	0.15
d	6.0	$85^\circ$	0.2	0.4

respectively. Before discussing the dependence of electron burst events on shock parameters, we first introduce the shock profiles produced by the self-consistent hybrid simulations with various shock parameters listed in Table 1. Figure 1 shows the evolution of magnetic field component  $B_z$  as a function of time  $t$  and space  $x$ . Subplots a–d correspond to cases a–d in Table 1, respectively. Cases a, b, and d in Figure 1 show very clear reforming shocks in which the shock front periodically collapse and develop on a timescale close to the ion cyclotron period. Case c, however, shows very weak variations in  $B_z$  (see Figure 2c also) due to low shock Mach number. Nevertheless the shock is still reforming: The  $B_z$  varies in a periodic manner (see also Figure 2c), the foot periodically extends far upstream due to upstream reflected ions. The shock propagates upstream from the right to the left of the simulation box as time  $t$  increases in a stepwise fashion. Shock reformation starts with the foot region extending far upstream with increasing magnetic field by reflecting up-

stream incoming ions, then the foot develops into a new steep ramp by accumulating the reflected ions, and then the previous shock ramp collapses. The shock reformation period is about  $1.6\Omega_{ci}^{-1}$ ,  $1.8\Omega_{ci}^{-1}$ ,  $2.0\Omega_{ci}^{-1}$ ,  $1.8\Omega_{ci}^{-1}$  for cases a–d, respectively. The shock propagation speeds are  $2.4v_A$ ,  $2.0v_A$ ,  $1.2v_A$ , and  $2.0v_A$  for cases a–d, respectively. It is seen that the shock propagates faster upstream (toward the left of simulation box) as the Mach number increases, and the variation of magnetic fields becomes more obvious.

[11] Figure 2 shows the variations of magnetic field strength ( $B_{max}$ ) as a function of time  $t$  for cases a–d. The dashed lines show the average values, and the dash-dot-dash lines are the values predicted by Rankine–Hugoniot relation. The Rankine–Hugoniot relation predicts smaller magnetic field strength than the average due to the magnetic overshoots. The  $B_{max}$  varies in the sawtooth manner at the shock reformation period and its variability depends strongly on the shock parameters. As an example,  $\Delta B_{max} / \langle B_{max} \rangle = 0.5$  for case a, but for case c  $\Delta B_{max} / \langle B_{max} \rangle = 0.05$ . Here  $\Delta B_{max}$  is the maximum change of  $B_{max}$  and  $\langle B_{max} \rangle$  is the average value of  $B_{max}$ . As the Mach number increases,  $\Delta B_{max}$  increases. It should be pointed out that the total cross shock potential drop varies in concert with the maximum magnetic field in 1D hybrid simulations (not shown here), and it changes in the same sawtooth manner as the maximum magnetic fields. The mean total cross shock potential drop

**Figure 1.** Relative magnetic field components  $B_z/B_0$  as a function of  $t$  and  $x$  for cases a–d.

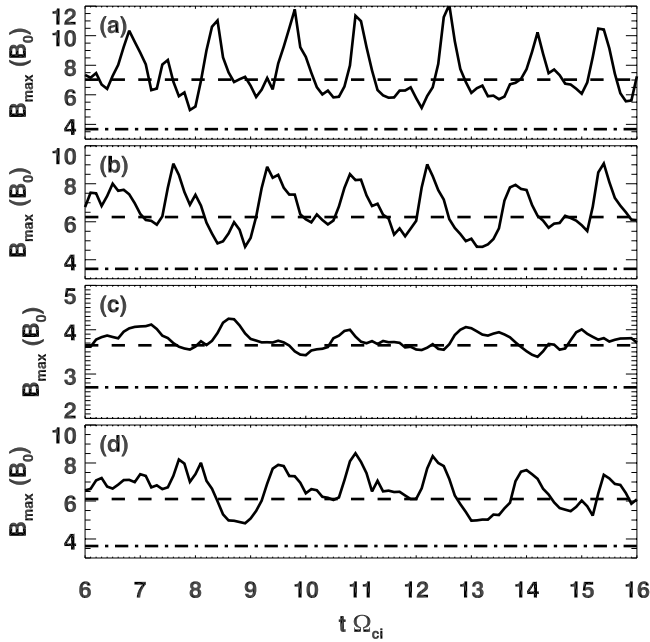


**Figure 2.** Variation of  $B_{\max}(t)$  for cases a–d. Dashed line: average values; dash-dot-dash line: Rankine–Hugoniot predictions.

over  $20\Omega_{ci}^{-1}$  for the cases a–d are 13.3, 7.5, 3.5 and 8.4, respectively.

### 3.2. Dependence of Electron Burst Events on Shock Parameters

[12] In this section, the dependence of electron burst events formed by shock reflected electrons on shock parameters will be discussed. We start with case a with shock parameters  $M_A = 7.4$ ,  $\beta_i = 0.15$ , and  $\beta_e = 0.2$ . Then we will show cases with decreased Mach number, but constant  $\beta_i = 0.15$ , and  $\beta_e = 0.2$ . Finally, we will discuss the case with larger ion plasma beta ( $\beta_i = 0.4$ ), otherwise identical shock parameters to case b in Table 1.

[13] Figure 3 shows phase space plots of electron energy versus  $x$  position at different times during shock reformation period for case a. It illustrates the dynamical formation of energetic electron bursts as in *Yuan et al.* [2007a]. The red lines show the  $B_z$  profile. At times  $14.0\Omega_{ci}^{-1}$ – $14.1\Omega_{ci}^{-1}$ , when the shock has a sharp ramp and the magnetic field strength reaches its maximum value, electrons are accumulated in the ramp region. The electron accumulation at the shock front happens because electrons travel different distance along the shock front: electrons that arrive earlier travel more deeply downstream since the maximum magnetic field is relatively small at that time, while newly arrived electrons travel shorter distances downstream. The accumulated electrons have small values of  $v_x$  and negative value of  $v_y$ , so they gain energy from the motional electric field (SDA). Near time  $14.3\Omega_{ci}^{-1}$  when the new ramp begins to form and the shock starts to collapse, the accumulated highly energetic electrons are released upstream and downstream at the same time. The newly released electrons travel back upstream at different parallel speeds, with the fast electrons traveling longer distances than the slow ones in the same time. This leads to “beam” features in the upstream

distributions by time-of-flight effects [*Filbert and Kellogg*, 1979], with one beam per burst. This motion leads to different energy versus  $x$  slopes for each event: an earlier burst always has a smaller energy versus  $x$  slope than a later one.

[14] The time-varying upstream electron distribution contours for case a are shown in Figure 4. The following features are observed: (1) The upstream electron distributions display obvious loss cone structures with a deficit (excess) of electrons at small (large) magnetic moments. (2) The loss cone angle changes cyclically with time. (3) The lack of electrons at low perpendicular speeds occurs due to magnetic mirroring, cross-shock potential effects, and the absence of electron leakage from downstream. Our previous simulations [*Yuan et al.*, 2007b] have demonstrated that electrons leaked from downstream will at least partially fill in the upstream loss cone. (4) In order for a reflected electron to escape far upstream, it must travel along the magnetic field with sufficiently high speeds to overcome the shock propagation. This introduces a parallel cut-off speed into the upstream distribution contours at the de Hoffmann–Teller speed, as shown by *Cairns* [1987]. Note that the de Hoffmann–Teller frame speed/cutoff speed ( $v_{HT} = (v_{\text{shock}} + V_{\text{in}})/\cos \theta_{bn}$ , where  $v_{\text{shock}}$  is the shock propagation speed) is  $6.6v_{\text{the}}$ . (5) The reflected electrons are often strongly concentrated in  $v_{\parallel}$  (above  $v_{HT}$ ) and  $v_{\perp}$  (above loss cone) and superposed on a loss cone, thereby forming a ring beam. The downstream leaked electrons also tend to form a ring beam [*Yuan et al.*, 2007b]. (6) The breadths in  $v_{\parallel}$  and  $v_{\perp}$  of the loss cone and ring beam structures change with time due to time-of-flight effects and intrinsic changes in  $v_{\parallel}$  and  $v_{\perp}$  with time of electrons escaping the shock. The time-of-flight works as follows: faster electrons arrive in the observational region early and create a ring beam at larger negative  $|v_{\parallel}|$ , while slower electrons arrive later and change the distribution function at smaller  $|v_{\parallel}|$ . (7) The electron distributions appear to have beams in  $v_{\parallel}$  as well as loss cone structures. These time-varying loss and ring beam features are expected to drive significant levels of time-varying waves.

[15] Figure 5 explicitly shows the average number density, parallel speed, the kinetic energy, and spread in parallel speed of beam as a function of time for case a. Their values cyclically change with time at the period of shock reformation due to the electron burst events. At times  $12.6\Omega_{ci}^{-1}$ ,  $14.2\Omega_{ci}^{-1}$ , and  $15.7\Omega_{ci}^{-1}$  when the fast part of shock reflected electrons enter the observation region, the number density, parallel speed, spread, and kinetic energy reach their maximum values, with  $n_{b,\max} / \langle n_b \rangle = 1.5$ ,  $v_{b,\max} / \langle v_b \rangle = 1.27$ ,  $v_{b,\max}^2 / \langle v_b^2 \rangle = 1.2$ , and  $\Delta v_{b,\max} / \langle \Delta v_b \rangle = 1.35$ . Here  $\langle \rangle$  means an average over a reformation period, and  $n_b = \int_{v_{HT}}^{\infty} dv_{\parallel} f_r(v_{\parallel})$ ,  $v_b = \int_{v_{HT}}^{\infty} dv_{\parallel} v_{\parallel} f_r(v_{\parallel})$ ,  $v_b^2 = \int_{v_{HT}}^{\infty} dv_{\parallel} v_{\parallel}^2 f_r(v_{\parallel})$ ,  $\Delta v_b = \sqrt{v_b^2 - \langle v_b \rangle^2}$ , respectively. Subscript “max” means the maximum over a reformation period. As the fast electrons pass through, the values of beam number density, speed, spread, and kinetic energy slowly decrease because the faster electrons have mostly passed through, leaving only slower electrons in the observation region.

[16] The electron energy spectra  $f_E(E)$  and reduced distribution functions  $f_r(v_{\parallel}) = \int dv_{\perp} 2\pi v_{\perp} f(v_{\perp}, v_{\parallel})$  observed at

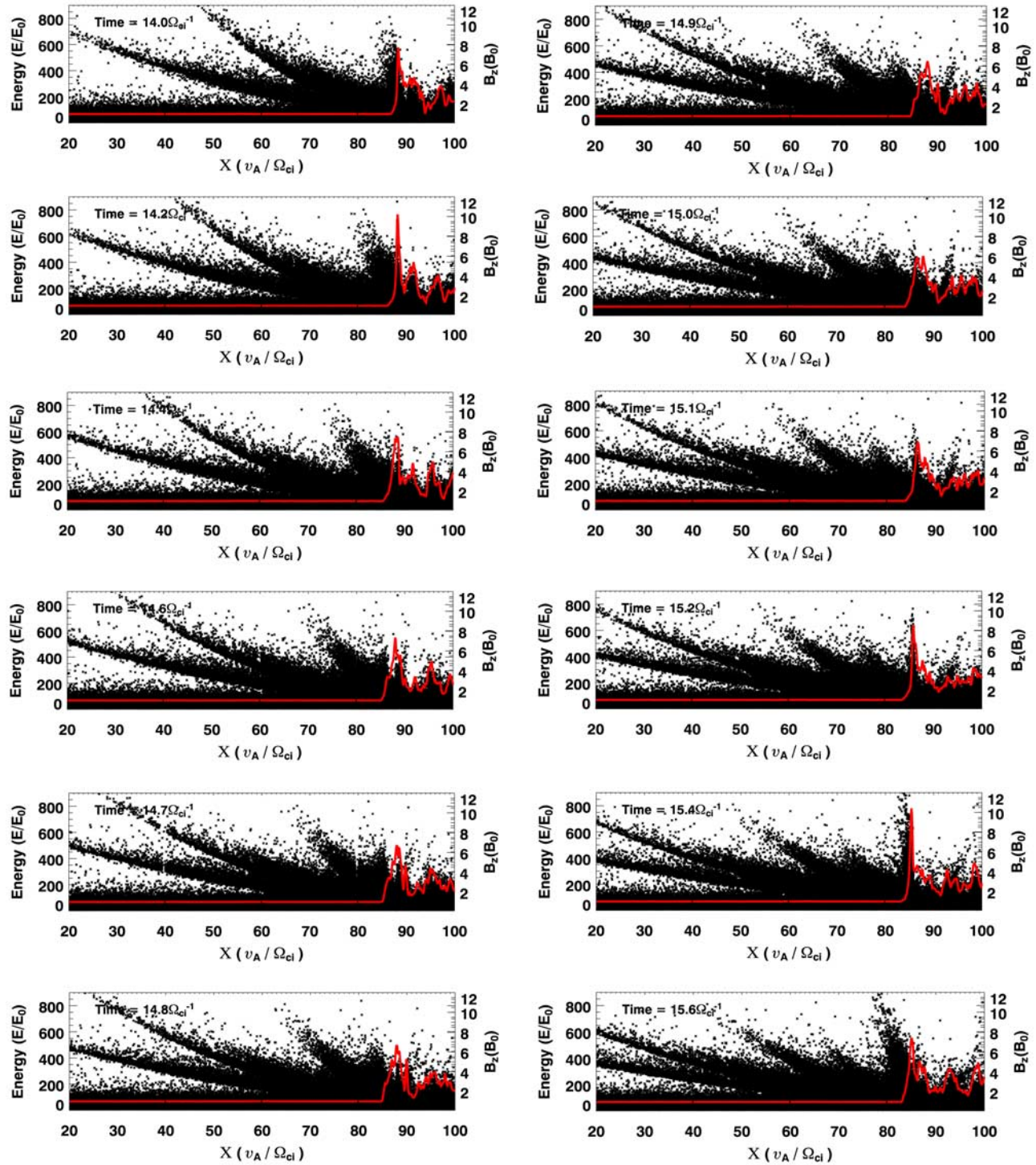


**Figure 3.** Energy-position phase space at different times for case a. The red lines are the  $B_z$  profiles.

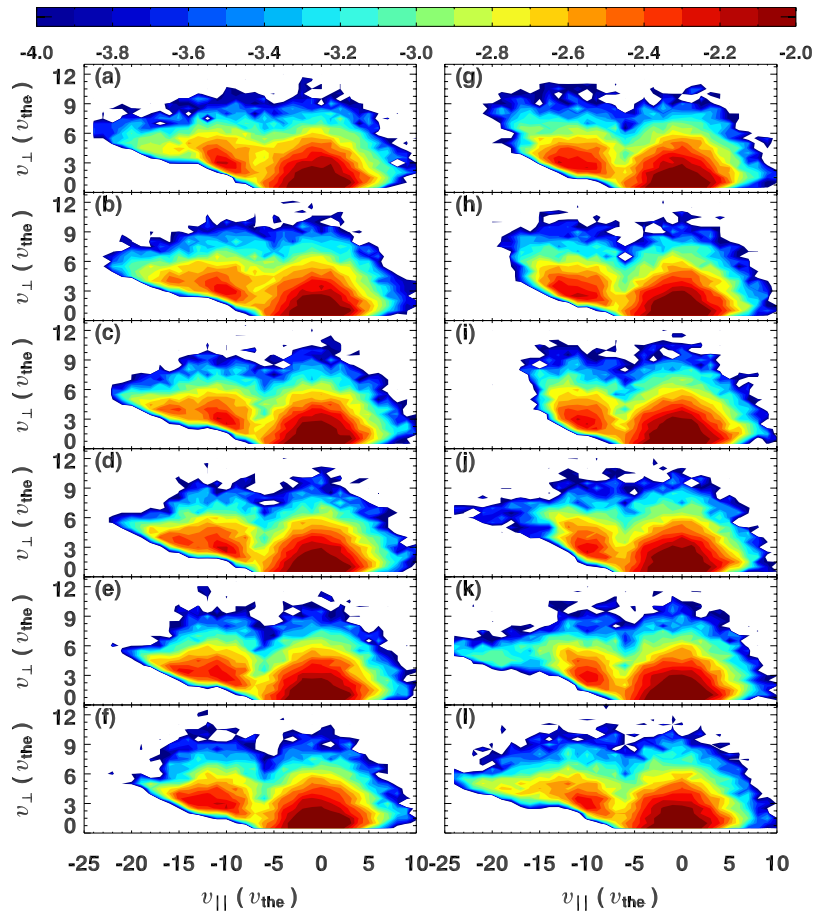


**Figure 4.** Electron distributions upstream of the shock for the same times as Figure 3 for case a.

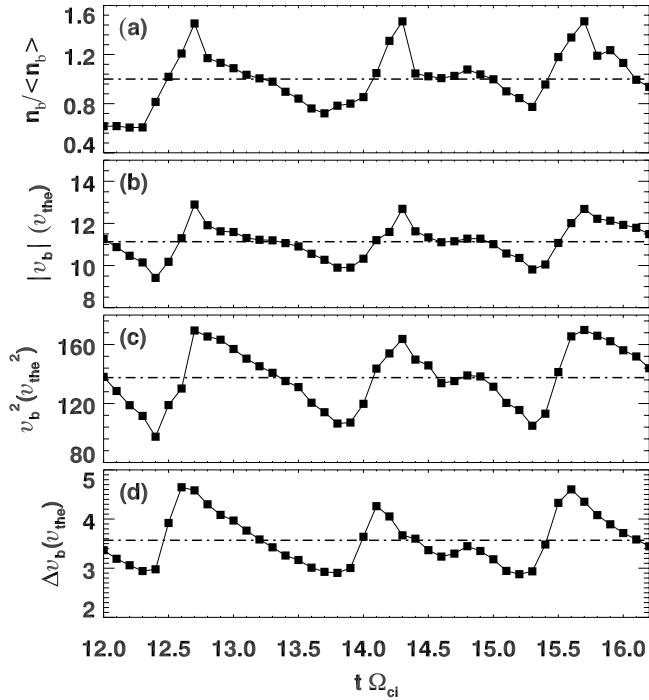


**Figure 5.** Time-varying beam (a) number density, (b) parallel speed, (c) kinetic energy, and (d) parallel spread for case a. The beam density is relative to the average over two reformation cycles. The dash-dot-dash lines show the average values.

different times are plotted in Figure 6. Clear time variations are also observed in the electron energy spectrum and reduced distribution functions, caused by the time-of-flight effects and intrinsic differences during the reformation

cycle. When the burst electrons first arrive in the observation region, a high-energy tail forms in the energy spectrum. The high-energy tail moves to smaller energies with time as the increasingly slow burst electrons pass through. In the reduced distribution functions, an electron beam is observed. As the burst electrons go through, the beam characteristics such as beam density, speed, and the available kinetic energy change with time, the beam extends to higher  $|v_{\parallel}|$  and the region with positive slope moves to lower parallel speeds.

[17] In order to investigate the dependence of electron burst events on Mach number, we decreased the Mach number in cases b, and c, leaving all the other parameters the same as case a. Figure 7 plots upstream electron distribution contours at different times during a reformation period for case b. Case b has a reforming shock with period of  $1.8\Omega_{ci}^{-1}$ ,  $\Delta B_{\max} / \langle B_{\max} \rangle = 0.4$ , and shock propagation speed  $2.0v_A$ . Similar to case a, the upstream electron distribution contours are not steady state. Instead, they display time-varying loss cone structures, and the breadths of the loss cone and ring beam structures in  $v_{\parallel}$  and  $v_{\perp}$  change with time also. However, due to the different shock propagation speed in case b, the de Hoffmann–Teller frame speed/cutoff speed ( $v_{HT} = 6.0$ ) is smaller. The loss cone contours extend less negative  $v_{\parallel}$  which will lead to lower average beam speed (see Figure 8). This is because the shock speed and the motional electric fields are smaller in case b. The loss cone angles in case b are larger since  $B_{\max}$  are smaller.

[18] The corresponding beam number density, speed, kinetic energy, and spread are shown in Figure 8. Once again, their values cyclically change with time at the period of shock reformation due to the electron burst events and changes in shock magnetic and potential profiles. However  $\langle n_b \rangle = 0.12n_0$ ,  $\langle v_b \rangle = 9.6v_{the}$ ,  $\langle v_b^2 \rangle = 105v_{the}^2$ , and  $\langle \Delta v_b \rangle = 3.0v_{the}$  for the case b, where  $n_0$  is the background electron

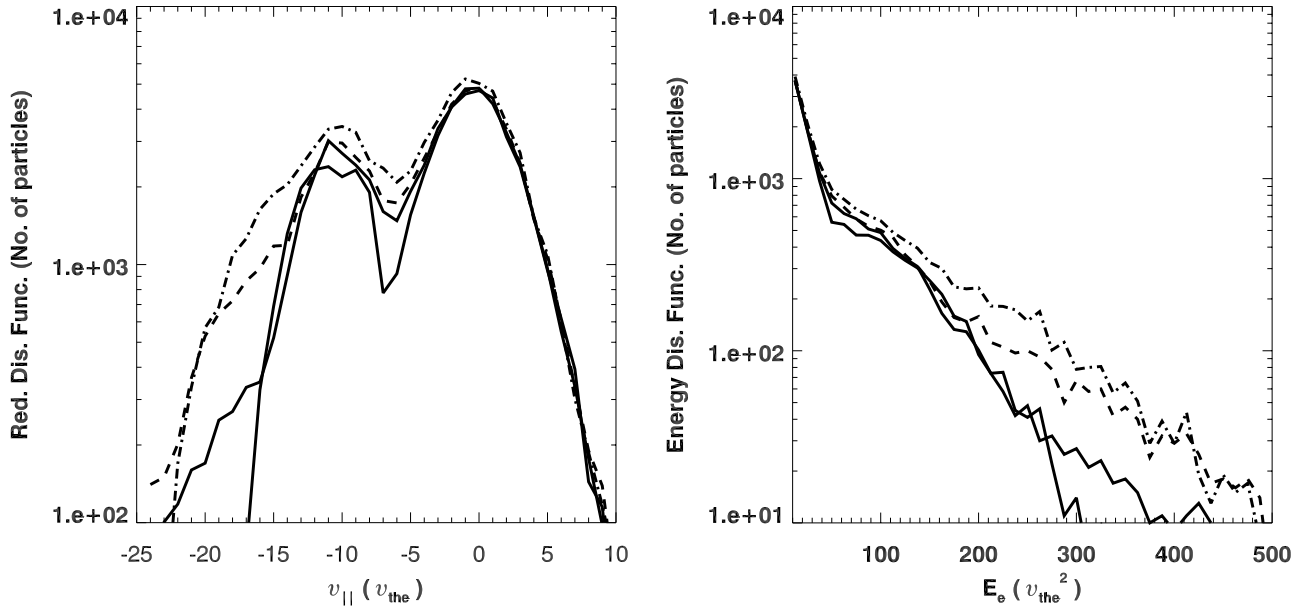


**Figure 6.** (Left) The reduced distribution functions and, (right) energy distribution functions for upstream electrons. Solid:  $t = 14.0\Omega_{ci}^{-1}$ ; dash:  $t = 14.1\Omega_{ci}^{-1}$ ; dash-dot-dash:  $t = 14.2\Omega_{ci}^{-1}$ ; dash-dot-dot-dash:  $15.2\Omega_{ci}^{-1}$ .

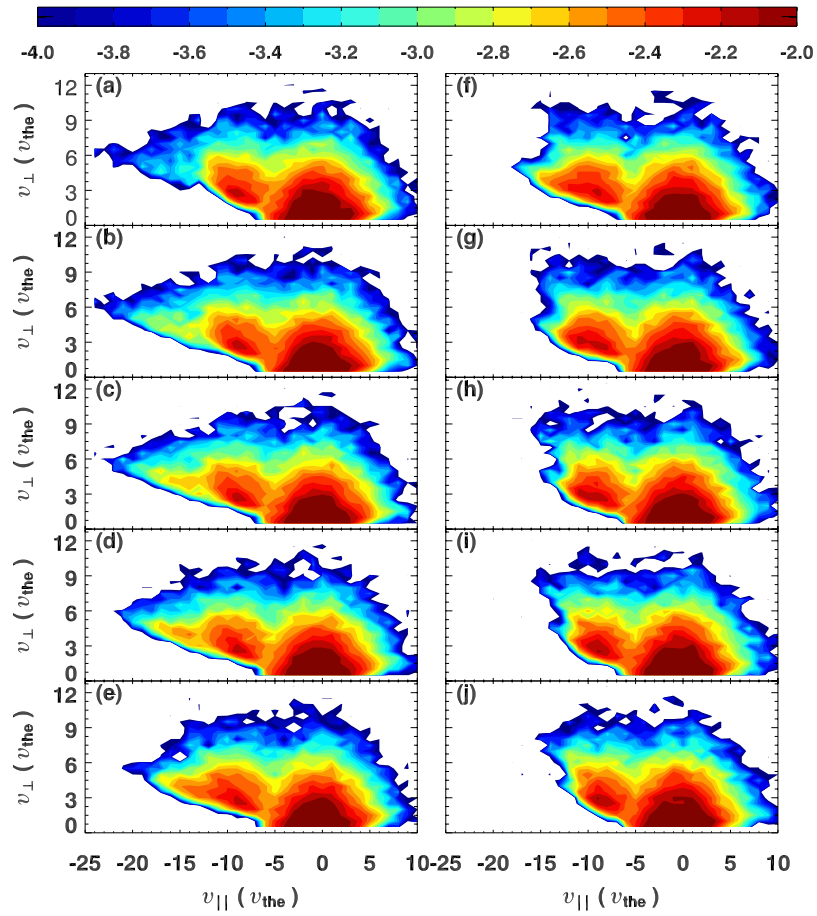


**Figure 7.** Electron distributions upstream of the shock at different times for case b.

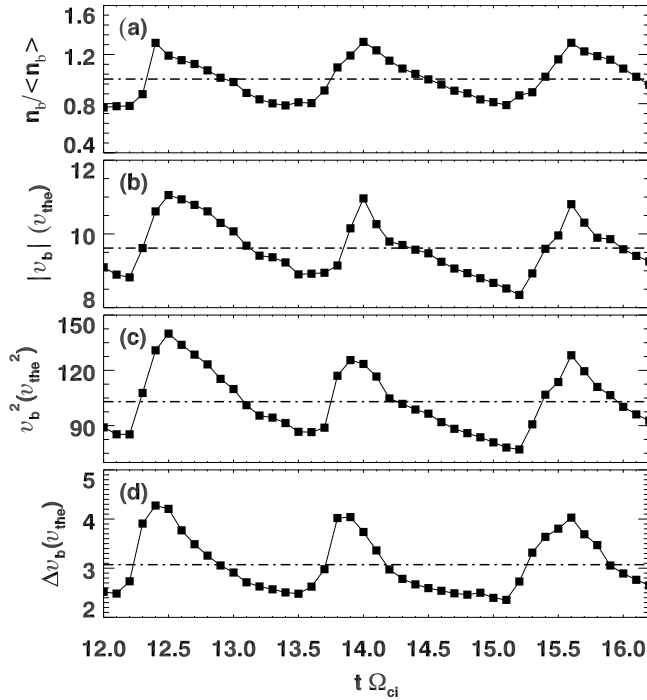


**Figure 8.** Time-varying beam (a) density, (b) speed, (c) kinetic energy, and (d) spread for case b. The beam density is relative to the average over two reformation cycles. The dash-dot-dash lines show the average values.

density at the observation window. The corresponding values for case a are  $0.16n_0$ ,  $11.2v_{the}$ ,  $140v_{the}^2$ ,  $3.75v_{the}$ , respectively. For case b, the maximum relative values are  $n_{b,max} / \langle n_b \rangle = 1.35$ ,  $v_{b,max} / \langle v_b \rangle = 1.2$ ,  $v_{b,max}^2 / \langle v_b^2 \rangle = 1.4$ , and  $\Delta v_{b,max} / \langle \Delta v_b \rangle = 1.5$  at times  $12.4\Omega_{ci}^{-1}$ ,  $13.9\Omega_{ci}^{-1}$  and  $15.4\Omega_{ci}^{-1}$  when the faster shock-reflected electrons enter the observation region. These are also different from the corresponding values for case a once again. As the fast electrons pass through, the values of beam density, speed, spread, and kinetic energy slowly decrease.

[19] In case c, we decreased Mach number further to  $M_A = 3.2$  but keep the other parameters constant. The shock is still reforming (see Figures 1 and 2), but now the variations of maximum magnetic field are very weak. The shock reformation period is about  $2.0\Omega_{ci}^{-1}$ ,  $\Delta B_{max} / \langle B_{max} \rangle = 0.05$ , and the shock propagation speed is  $1.2v_A$ . Contrary to cases a and b, now the predicted electron distribution contours at different times are quasi-steady with only small differences in the large negative  $v_{||}$  region (see Figure 9). The loss cone angle, the envelope of the loss cone and ring beam structures are almost identical at different times. This means that the shock reflects the upstream incoming electrons continuously, which is quite different from the burstiness observed for actively reforming shocks.

[20] In order to compare the distribution contours of case c with a steady-state shock, we calculated the distribution functions using Yuan *et al.*'s [2007b] test particle code for steady-state shock that had the overshoots  $B_{max}$  and  $\phi_{max}$  obtained by averaging the maximum values of  $B_z/B_0$  over a reformation period. It is found that the predicted upstream distribution contours are almost same. This shows that case

c's weakly reforming shocks reflects the upstream incoming electrons almost continuously and in a very similar to the steady-state shock.

[21] The plots of beam number density, speed, kinetic energy, and parallel spread as a function of time (Figure 10) show that an essentially continuous, quasi-steady, beam is formed in case c. In contrast to the electron beams in cases a and b, now the values  $\langle n_b \rangle = 0.05n_0$ ,  $\langle v_b \rangle = 7v_{the}$ ,  $\langle v_b^2 \rangle = 52v_{the}^2$ , and  $\langle \Delta v_b \rangle = 1.9 v_{the}$  are much smaller. The maximum relative values are  $n_{b,max} / \langle n_b \rangle = 1.05$ ,  $v_{b,max} / \langle v_b \rangle = 1.02$ ,  $v_{b,max}^2 / \langle v_b^2 \rangle = 1.02$ , and  $\Delta v_{b,max} / \langle \Delta v_b \rangle = 1.1$  at times  $12.8\Omega_{ci}^{-1}$  and  $15.0\Omega_{ci}^{-1}$  when the fast part of shock reflected electrons enter the observation region. These variations are also much smaller than the corresponding variations for cases a and b.

[22] So far, we have concentrated on the effects of varying the Mach number. In case d, we use a higher plasma beta ( $\beta_i = 0.4$ ) but keep the other parameters the same as in case b. Now the predicted shock profiles reform with period of  $2.0\Omega_{ci}^{-1}$ ,  $\Delta B_{max} / \langle B_{max} \rangle = 0.3$ , so that increasing  $\beta_i$  increases the reformation period and decreases  $\Delta B_{max} / \langle B_{max} \rangle$ . Figure 11 shows the corresponding electron distribution at different times. Similar to case b, time-varying electron distributions are observed with the loss cone angles and envelopes cyclically changing with time. Compared with case b, the envelope of the loss cone contours extends to lower parallel and perpendicular speeds, and the average loss cone angle is larger due to the smaller maximum magnetic field.

[23] The beam number density, speed, kinetic energy, and spread as a function of time for case d are shown in Figure 12. Now  $\langle n_b \rangle = 0.14n_0$ ,  $\langle v_b \rangle = 9v_{the}$ ,  $\langle v_b^2 \rangle = 110v_{the}^2$ ,  $\langle \Delta v_b \rangle = 3v_{the}$ . The maximum relative values are  $n_{b,max} / \langle n_b \rangle = 1.3$ ,  $v_{b,max} / \langle v_b \rangle = 1.2$ ,  $v_{b,max}^2 / \langle v_b^2 \rangle = 1.35$ , and  $\Delta v_{b,max} / \langle \Delta v_b \rangle = 1.5$  at times  $12.6\Omega_{ci}^{-1}$ ,  $14.2\Omega_{ci}^{-1}$  and  $15.7\Omega_{ci}^{-1}$  when the fast part of shock reflected electrons enter the observation region. These variation are almost identical to those for case b.

[24] Finally, the reflection efficiencies for cases a–d, defined as the ratio of reflected electrons to the background upstream incoming electrons in the observation window are plotted in Figure 13. It is seen that the reflection efficiencies change cyclically with time at the shock reformation period for the cases a, b and d, which means the upstream incoming electrons are reflected nonuniformly with time. However, for case c, the reflection efficiency is almost constant during the shock reformation period, with only about 1% variation, very different from cases a, b, and d. The upstream incoming electrons are almost reflected continuously even the shock front is cyclically changing with time at the period of shock reformation.

#### 4. Summary and Discussion

[25] In this paper we extended our previous work [Yuan *et al.*, 2007a] to investigate the dependence of upstream electron burst events on the shock parameters  $\beta$  and  $M_A$ . The test particle approximation is made for superthermal halo electrons and the shock profiles are self-consistently produced by one-dimensional hybrid simulations. The test particle electron trajectories are exactly traced by numeri-

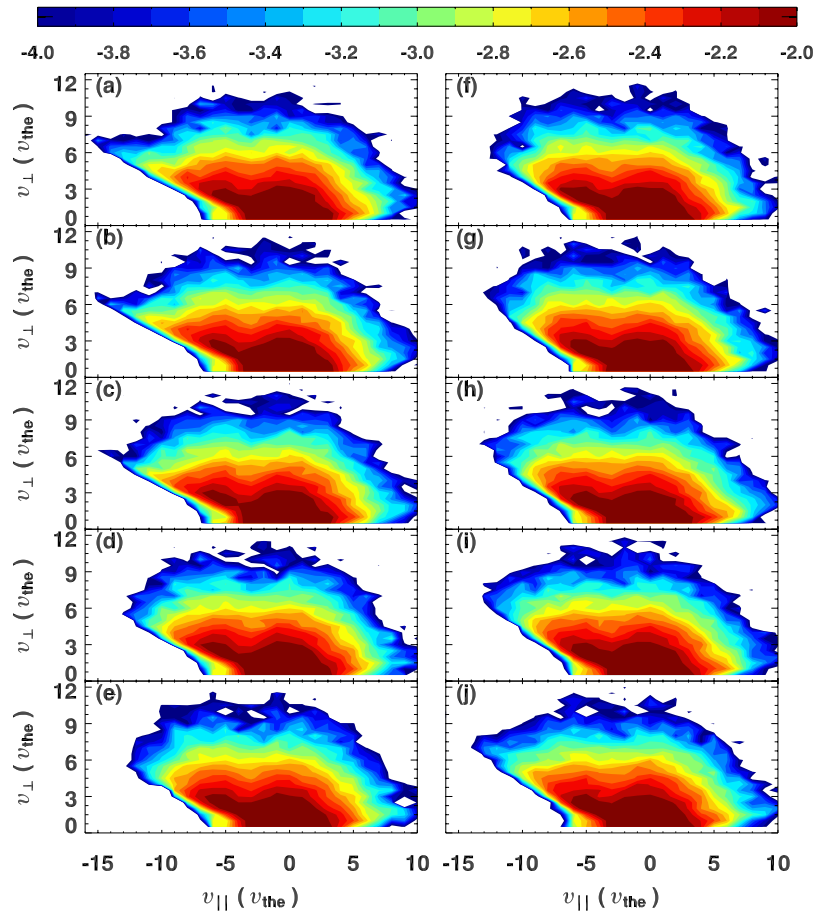


**Figure 9.** Electron distributions upstream of the shock at different times for case c.

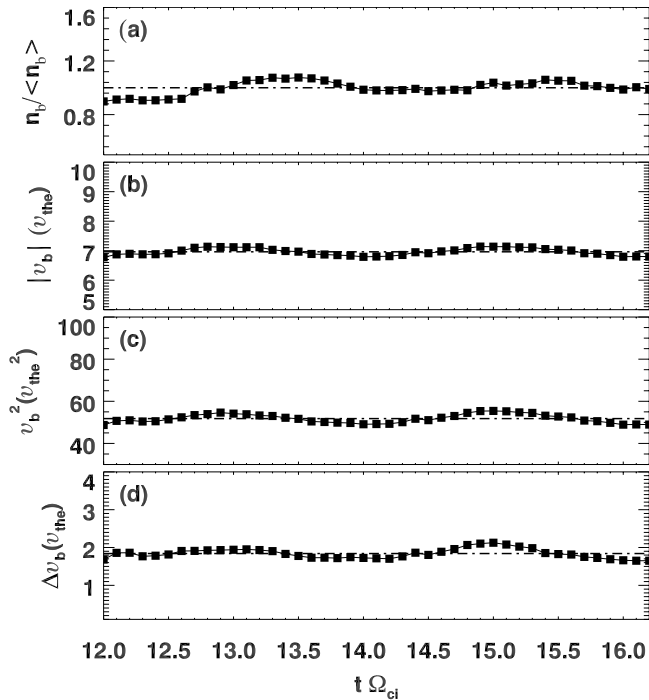


**Figure 10.** Electron beam (a) density, (b) speed, (c) kinetic energy, and (d) spread as function of time for case c. The beam density is relative to the average over two reformation cycles. The dash-dot-dash lines show the average values.

cally integrating the full equations of motion (including gyromotion) using a seventh-order Runge–Kutta method.

[26] The test particle calculations show that the upstream energetic electron burst events and the resulting electron beam features depend strongly on the shock parameters. Specifically, for high Mach number, low  $\beta$ , collisionless shocks (case a), the upstream incoming electrons are reflected nonuniformly in time by the shock fronts, with bursty energetic electron events observed upstream of the shock. This behavior is different from steady-state shocks in which the upstream incoming electrons are continuously reflected. These findings are consistent with *Lembege and Savoini's* [2002] particle in cell simulation results. They also agree with *Burgess's* [2006] work which shows that superthermal electrons can be scattered by dynamical shock ripples, even without strong electron scale fluctuations.

[27] Detailed examination shows that the cyclical energetic electron events begin with the accumulation of incoming electrons in the shock front region during phases in which the new ramp develops and sharpens. Then a burst of electrons is released upstream and downstream simultaneously after the electrons gain enough energy and the ramp collapses. Due to the dispersion caused by the time-of-flight effects, some mixing of electrons from different burst events is observed in phase space and leads to different electron energy versus  $x$  slopes for each event. The upstream electron distributions display time-varying loss cone, beam and ring beam structures with the loss cone angle and the ranges and centers in  $v_{\parallel}$  and  $v_{\perp}$  changing with time. The beam density, speeds, available kinetic energy, and the positive slope in the reduced distribution functions change

by factors of  $\sim 2$ – $4$ , and the region of positive slope changes.

[28] Decreasing the shock Mach number to 6.0 (case b) from 7.4 (case a), the hybrid simulations predict a reforming shock with a similar reformation process to case a, but the value of  $\Delta B_{\max}/\langle B_{\max} \rangle$  is reduced to 1.5. The energetic electron burst events are still observed, but the average beam density, speed, kinetic energy, and spread become smaller and the relative values  $n_{b,\max}/\langle n_b \rangle$ ,  $v_{b,\max}/\langle v_b \rangle$ ,  $v_{b,\max}^2/\langle v_b^2 \rangle$ , and  $\Delta v_{b,\max}/\langle \Delta v_b \rangle$  become smaller also. Decreasing the shock Mach number further to 3.2 lead to shock reformation still, but the variations of the shock profile become very weak and the electron burst events disappear. Instead, the electrons are almost continuously reflected by the shock front and the upstream observed distributions contours are essentially time independent. An almost continuous electron beam is observed. Comparison with the beam characteristics calculated for test particle reflecting of a steady-state shocks with the same  $B_{\max}$  and overshoots show that the beam is qualitatively almost the same. Increasing plasma beta (providing the shock is still reforming) has minor effects on the upstream electron beam features.

[29] When increasing the Mach number, the shock profiles predicted by the hybrid code have higher maximum magnetic field, obvious variations of the maximum magnetic field during the shock reformation period, and higher shock speed in the simulation frame. The cyclical electron burst events are observed, and the reflected electrons have higher energy in the simulation frame (NIF frame). The beam density, speeds, available kinetic energy, and spreads change by factors of  $\sim 2$ – $4$ . The beam density decrease, and the beam speed, and available kinetic energy increase. These features agree with the theoretical analysis [*Wu, 1984; Leroy and Mangeney, 1984*] and the numerical simulations [*Krauss-Varban et al., 1989*].

[30] In conclusion, the dependences of upstream electron reflection on shock parameters ( $M_A$  and  $\beta$ ) can be explained as follows: When the shock Mach number is high, the variations of magnetic field  $\Delta B_{\max}/\langle B_{\max} \rangle$ , and cross shock potential drop during the reformation period is large. More upstream incoming electrons can be transmitted to the downstream region during the shock collapse phase because the total cross shock potential drop and the maximum magnetic field are smaller, and electrons spend more time inside the shock transition region because the magnetic field and cross shock potential extend far upstream and the shock transition region becomes wider. As time goes on, the total cross shock potential drop and maximum magnetic field increase, electrons which can be transmitted downstream by the previous shock fields feel the increasing of maximum magnetic field and cross shock potential, and accumulate at the shock front region. When the new sharp shock ramp develops, those accumulated electrons eventually released upstream and downstream at the same time. As shock Mach decreases, the variations of magnetic field and cross shock potential drop during the shock reformation period become weaker (see Figure 14), the upstream incoming electrons only feel little changes on the shock fields, so the change of reflection ratios is very small. This small change of electron reflection is hard to be observed in the distribution functions, so we observe a steady-state electron beams, and loss

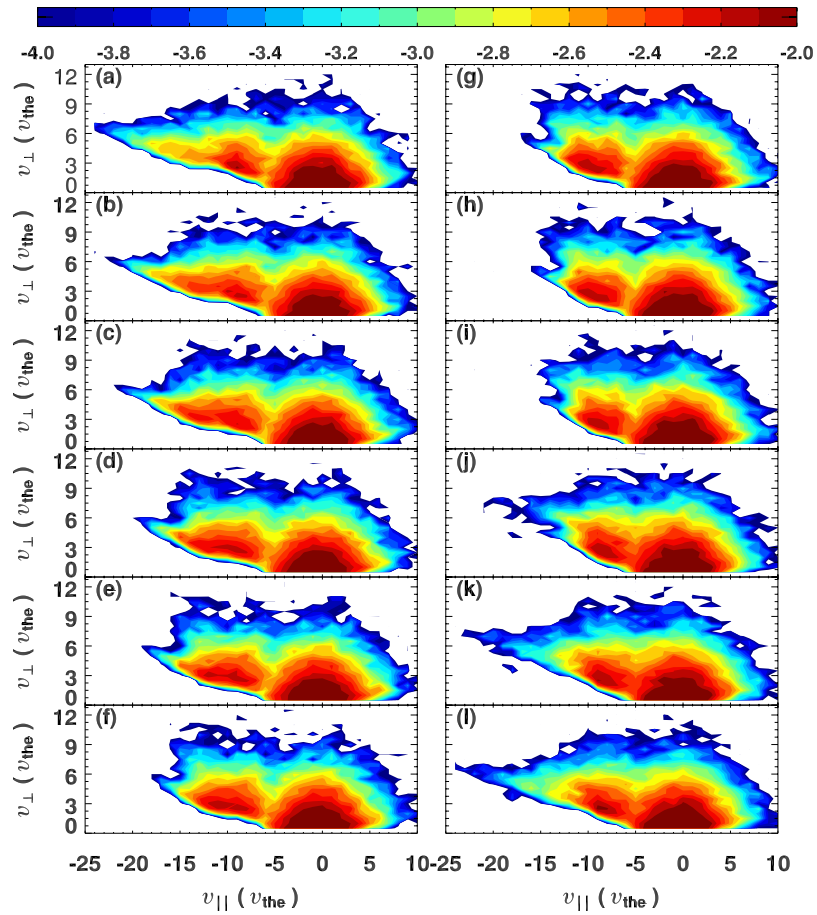


**Figure 11.** Electron distributions upstream of the shock at different times for case d.

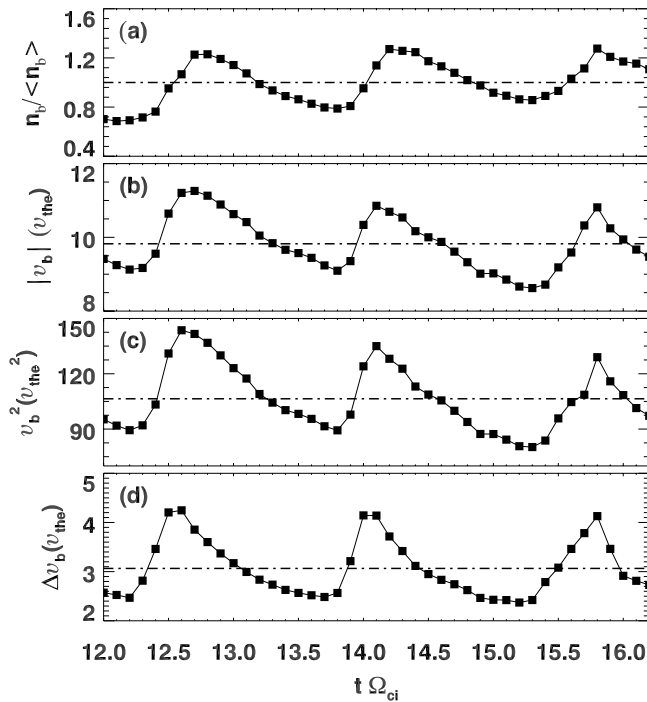


**Figure 12.** Electron beam (a) density, (b) speed, (c) kinetic energy, and (d) spread as function of time for case d. The beam density is relative to the average over two reformation cycles. The dash-dot-dash lines show the average values.

cone angles in the upstream distributions are time steady also. Little changes in plasma beta ( $\beta$ ) for the high Mach number shocks don't change the variations of magnetic field

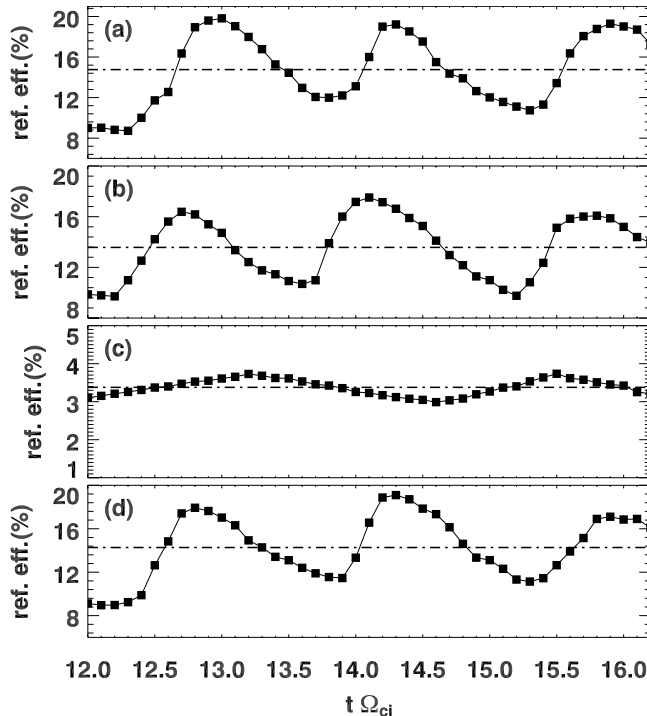


**Figure 13.** Variation of reflection efficiency as a function of time  $t$  for cases a–d.

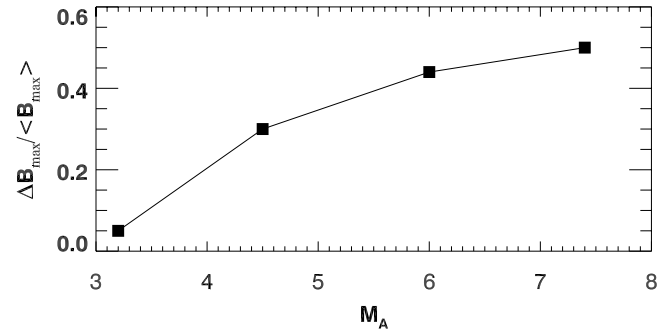


**Figure 14.** Change of  $\Delta B_{\max}/\langle B_{\max} \rangle$  as function of shock Mach number.

and cross shock potential drop too much, so burst electron events are still observed in upstream region.

[31] Finally, the beam, loss cone, and ring beam features found in upstream distributions have parallel/perpendicular gradients in the electron distributions and so might drive waves [Yuan *et al.*, 2007b]. The electron beam-driven plasma instabilities upstream of the shock have been studied by many researchers [Filbert and Kellogg, 1979; Cairns, 1987; Fitzenreiter *et al.*, 1990; Lobzin *et al.*, 2005]. This paper shows that the observed electron beam is time-varying or steady-state depending on the shock parameters. The time-varying electron beams will lead to different wave growth rates, amounts of available free energy, and possibly even different wave modes from the steady-state beams as shown by Hewitt and Melrose [1984], Cairns and Fung [1988] and Lobzin *et al.* [2005], and should be studied further.

[32] **Acknowledgments.** This work was funded by the Australian Research Council and Canada Space Agency. The simulation has been enabled by the use of WestGrid computing resources ([www.westgrid.ca](http://www.westgrid.ca)) and the facilities of the Shared Hierarchical Academic Research Computing Network SHARCNET:[www.sharcnet.ca](http://www.sharcnet.ca)).

[33] Amitava Bhattacharjee thanks Michael Gedalin and another reviewer for their assistance in evaluating this paper.

## References

- Anderson, K. A. (1969), Energetic electrons of terrestrial origin behind bow shock and upstream in solar wind, *J. Geophys. Res.*, *74*, 95.
- Anderson, K. A. (1981), Measurements of bow shock particles far upstream from the Earth, *J. Geophys. Res.*, *86*, 4445.
- Anderson, K. A., R. P. Lin, F. Martel, C. S. Lin, G. K. Parks, and H. Réme (1979), Thin sheets of energetic electrons upstream from the Earth's bow shock, *Geophys. Res. Lett.*, *5*, 404.
- Burgess, D. (2006), Simulation of electron acceleration at collisionless shocks: The effects of surface fluctuations, *Astrophys. J.*, *653*, 316.
- Cairns, I. H. (1987), The electron distribution function upstream from the Earth's bow shock, *J. Geophys. Res.*, *92*, 2315.
- Cairns, I. H., and S. F. Fung (1988), Growth of electron plasma waves above and below fp in the electron foreshock, *J. Geophys. Res.*, *93*, 7307.
- Evans, D. J., K. Murugesan, S. Sekar, and H. M. Kim (2006), Non-linear singular systems using RK-Butcher algorithms, *Int. J. Comput. Math.*, *83*(1), 131.
- Fan, C., Y. Gloeckler, and J. A. Simpson (1964), Evidence for  $\geq 30$  keV electrons accelerated in the shock transition region beyond the Earth's magnetospheric boundary, *Phys. Rev. Lett.*, *13*, 149.
- Filbert, P. C., and P. J. Kellogg (1979), Electrostatic noise at the plasma frequency beyond the Earth's bow shock, *J. Geophys. Res.*, *84*, 1639.
- Fitzenreiter, R. J., J. D. Scudder, and A. J. Klimas (1990), Three-dimensional analytical model for the spatial variation of the foreshock electron distribution function: Systematics and comparisons with ISEE observations, *J. Geophys. Res.*, *95*, 4155.

- Hada, T., M. Oonishi, B. Lembège, and P. Savoini (2003), Shock front nonstationarity of supercritical perpendicular shocks, *J. Geophys. Res.*, *108*(A6), 1233, doi:10.1029/2002JA009339.
- Hellinger, P., P. Trávníček, and H. Matsumoto (2002), Reformation of perpendicular shocks: Hybrid simulations, *Geophys. Res. Lett.*, *29*(24), 2234, doi:10.1029/2002GL015915.
- Hellinger, P., P. Trávníček, B. Lembège, and P. Savoini (2007), Emission of nonlinear whistler waves at the front of perpendicular supercritical shocks: Hybrid versus full particle simulations, *Geophys. Res. Lett.*, *34*, L14109, doi:10.1029/2007GL030239.
- Hewitt, R. G., and D. B. Melrose (1984), The loss-cone driven instability for Langmuir waves in an unmagnetized plasma, *Sol. Phys.*, *96*, 157.
- Hoshino, M., and N. Shimada (2002), Nonthermal electrons at high Mach number shocks: Electron shock surfing acceleration, *Astrophys. J.*, *572*, 880.
- Johns, C., and R. P. Lin (1992), The derivation of parent electron spectra from bremsstrahlung hard X-ray spectra, *Sol. Phys.*, *137*, 121.
- Knock, S. A., I. H. Cairns, P. A. Robinson, and Z. Kuncic (2001), Theory of type II radio emission from the foreshock of an interplanetary shock, *J. Geophys. Res.*, *106*, 25041.
- Knock, S. A., I. H. Cairns, P. A. Robinson, and Z. Kuncic (2003), Theoretically predicted properties of type II radio emission from an interplanetary foreshock, *J. Geophys. Res.*, *108*(A3), 1126, doi:10.1029/2002JA009508.
- Krauss-Varban, D. (1994), Electron acceleration at nearly perpendicular collisionless shocks: 3. Downstream distributions, *J. Geophys. Res.*, *99*, 2537.
- Krauss-Varban, D., and D. Burgess (1991), Electron acceleration at nearly perpendicular collisionless shocks: 2. Reflection at curved shocks, *J. Geophys. Res.*, *96*, 143.
- Krauss-Varban, D., D. Burgess, and C. S. Wu (1989), Electron acceleration at nearly perpendicular collisionless shocks: 1. One-dimensional simulations without electron scale fluctuations, *J. Geophys. Res.*, *94*, 15,089.
- Krasnoselskikh, V. V., B. Lembège, P. Savoini, and V. V. Lobzin (2002), Nonstationarity of strong collisionless quasiperpendicular shocks: Theory and full particle numerical simulations, *Phys. Plasmas*, *9*, 1192.
- Kuncic, Z., I. H. Cairns, and S. A. Knock (2004), A Quantitative model for terrestrial foreshock radio emissions: 1. Predicted properties, *J. Geophys. Res.*, *109*, A02108, doi:10.1029/2003JA010125.
- Lembège, B., and P. Savoini (1992), Nonstationarity of a two-dimensional quasiperpendicular supercritical collisionless shock by self-reformation, *Phys. Fluids*, *B4*, 3533.
- Lembège, B., and P. Savoini (2002), Formation of reflected electron bursts by the nonstationarity and nonuniformity of a collisionless shock front, *J. Geophys. Res.*, *107*(A3), 1037, doi:10.1029/2001JA900128.
- Leroy, M. M., and A. Mangeney (1984), A theory of energization of solar wind electrons by the Earth's bow shock, *Ann. Geophys.*, *2*, 499.
- Lobzin, V., V. V. Krasnoselskikh, S. Schwartz, I. H. Cairns, B. Lefevre, and P. Decreau (2005), Generation of downshifted oscillations in the electron foreshock: A loss cone instability, *Geophys. Res. Lett.*, *32*, L18101, doi:10.1029/2005GL023563.
- Lobzin, V. V., V. V. Krasnoselskikh, J.-M. Bosqued, J.-L. Pinon, S. J. Schwartz, and M. Dunlop (2007), Nonstationarity and reformation of high-Mach-number quasiperpendicular shocks: Cluster observations, *Geophys. Res. Lett.*, *34*, L05107, doi:10.1029/2006GL029095.
- Lowe, R. E., and D. Burgess (2000), Energetic electrons downstream of Earth bow shock: Simulations of acceleration by shock structure, *Geophys. Res. Lett.*, *27*, 3249.
- Parks, G. K., et al. (1981), Upstream particle spatial gradients and plasma waves, *J. Geophys. Res.*, *86*, 4343.
- Scholer, M., I. Shinohara, and S. Matsukiyo (2003), Quasi-perpendicular shocks: Length scale of the cross-shock potential, shock reformation, and implication for shock surfing, *J. Geophys. Res.*, *108*(A1), 1014, doi:10.1029/2002JA009515.
- Shimada, N., and M. Hoshino (2000), Strong electron acceleration at high Mach number shock waves: Simulation study of electron dynamics, *Astrophys. J.*, *543*, L67.
- Shu, C.-W. (1997), Essentially non-oscillatory and weighted essentially non-oscillatory schemes for hyperbolic conservation laws, *ICAS Report No. 97-65*, NASA-CR/97-206253.
- Vandas, M. (1989a), Acceleration of electrons by a nearly perpendicular shock: A comparison between observation and theory, *Bull. Astron. Inst. Czechoslov.*, *40*, 175.
- Vandas, M. (1989b), Acceleration of electrons by a nearly perpendicular shock: The dynamics of electron motion, *Bull. Astron. Inst. Czechoslov.*, *40*, 189.
- Veltri, P., A. Mangeney, and J. D. Scudder (1990), Electron heating in quasi-perpendicular shocks: A Monte Carlo simulation, *J. Geophys. Res.*, *95*, 14,939.
- Wu, C. S. (1984), A fast Fermi process: Energetic electrons accelerated by a nearly perpendicular bow shock, *J. Geophys. Res.*, *89*, 8857.
- Yuan, X., I. H. Cairns, and P. A. Robinson (2007a), Simulation of energetic electron bursts upstream of reforming shocks, *Astrophys. J.*, *671*, 439.
- Yuan, X., I. H. Cairns, P. A. Robinson, and Z. Kuncic (2007b), Effects of overshoots on electron distributions upstream and downstream of quasiperpendicular collisionless shocks, *J. Geophys. Res.*, *112*, A05108, doi:10.1029/2006JA011684.
- Yuan, X., I. H. Cairns, and P. A. Robinson (2007c), Hybrid simulation of reforming shocks with finite electron mass and pressure tensor effects, *Geophys. Res. Lett.*, *34*, L02101, doi:10.1029/2006GL028447.

I. H. Cairns, School of Physics, University of Sydney, Sydney, NSW 2006, Australia. (cairns@physics.usyd.edu.au)

R. Rankin, Department of Physics, University of Alberta, Edmonton, AB T6G 2G7, Canada. (rankin@phys.ualberta.ca)

L. Trichtchenko and X. Yuan, Geomagnetic Laboratory, Natural Resource Canada, Ottawa, ON K1A 0Y3, Canada. (lrichtc@nrcan.gc.ca; xyuan@nrcan.gc.ca)